

Adsorption and Electrodeposition on SnO₂ and WO₃ Electrodes in 1 M LiClO₄/PC

In Situ Light Scattering and *In Situ* Atomic Force Microscopy Studies

J. Isidorsson,^a T. Lindström,^a C. G. Granqvist,^{a,*} and M. Herranen^b

^aDepartment of Materials Science, ^bDepartment of Inorganic Chemistry, The Ångström Laboratory, Uppsala University, SE-751 21 Uppsala, Sweden

A novel spectroscopic *in situ* light scattering technique was used with *in situ* atomic force microscopy (AFM) to study electrode surfaces subjected to adsorption and electrodeposition. Tin dioxide and tungsten trioxide were used as electrodes in a 1 M LiClO₄/propylene carbonate electrolyte. Both *in situ* methods showed the same increase in surface roughness immediately after the electrode was immersed in the electrolyte. The onset potential for electrodeposition could be determined; its specific value depended on the film composition as well as on the composition and purity of the electrolyte. A potential step technique revealed a progressive growth of the first electrodeposited layer. The growth mode after fully developed electrodeposition was characterized by a preferential growth of large crystals, evident from light scattering as well as AFM. Our experimental techniques make it possible to determine whether electrodeposition or electrochromism, due to electrochemical insertion of ionic species, dominates the observed modulation of the optical properties. The deposited layer was investigated using infrared spectroscopy, X-ray diffraction, and X-ray photoelectron spectroscopy. Although the composition of this layer cannot be stated conclusively, it most likely contains lithium alkyl carbonate species.

© 2000 The Electrochemical Society. S0013-4651(99)08-124-0. All rights reserved.

Manuscript submitted August 30, 1999; revised manuscript received February 24, 2000.

Electrochromic electrodes rely on reversible electrochemical insertion and extraction of ions in a host material, thereby changing the color of the electrode.^{1,2} These processes can only be accomplished within a well-defined potential range. Practical applications often employ aprotic electrochemical systems capable of providing a wide potential window. Outside the potential window, the electrolyte decomposes and precipitates on the electrode. Such a deposited layer affects the optical behavior of the electrode in a generally undesirable way. Consequently, it is important to be able to establish if electrodeposition takes place, as well as to determine the specific onset potential of this phenomenon.

In this work, we investigate the initial adsorption taking place on an electrode immersed in an electrolyte, as well as the potential range that can be used for electrochemical experiments to avoid the onset of electrodeposition. The methods applied are *in situ* spectroscopic light scattering under electrochemical polarization and *in situ* atomic force microscopy (AFM). The examined electrochromic electrodes are sputter deposited tin dioxide³ (SnO₂) and tungsten trioxide⁴ (WO₃) immersed in an anhydrous electrolyte of 1 M LiClO₄ dissolved in propylene carbonate (PC).

The section on Theory outlines the approach chosen to describe the surface morphology, as well as the principle of the light scattering measurements. The Experimental section summarizes experimental details concerning the preparation and analysis of the SnO₂ and WO₃ films. The section on Adsorption on the surface considers the adsorption when the electrode is immersed in the electrolyte, as detected by light scattering and AFM. The section on Onset of Electrodeposition describes the onset of electrodeposition and the growth of the deposited layer as seen by light scattering. The section on Growth of the electrodeposited layer considers the growth of this layer by analyzing the chronoamperometric response and AFM data. The composition of the surface layers is discussed in the section on Film composition. The Conclusions section summarizes the work.

Table I is a guide to the different mechanisms and properties that have been studied in this work; it specifies the techniques to probe the characteristics and the corresponding potential ranges, and it states in what section of this paper the discussion can be found. Clearly, we have chosen to describe our work starting from the virgin electrode state and then going successively toward lower applied

potentials, thereby studying the pertinent reactions at different potentials and charge levels.

Theory

Surface morphology.—The morphology of an interface can be described by a topographic function, involving a large amount of data, but because of the complex nature of randomness, the interface is usually simplified using statistical parameters. Typically, both vertical and lateral descriptors are used. Most common are the interface width, often represented by the root-mean-square (rms) roughness value δ , and the lateral correlation length ξ , which gives the average distance between features in the surface profile within which the surface variations are correlated. The morphology of a surface can also be described by power spectral density (PSD) functions. The PSD function $g(\mathbf{K})$, where \mathbf{K} is the spatial wave vector with units of inverse length, is a measure of both vertical and lateral properties of a surface. It is found directly from a surface profile by taking the square of the Fourier transform of the topographical profile $z(\mathbf{r})$. The pertinent expression in the two-dimensional case, with $\mathbf{r} = (x, y)$, is⁵⁻⁷

$$g(\mathbf{K}) = \lim_{A \rightarrow \infty} \frac{1}{A} \left| \int z(\mathbf{r}) \exp(i\mathbf{K} \cdot \mathbf{r}) d\mathbf{r} \right|^2$$

$$\approx \frac{d_x d_y}{NM} \left| \sum_{n=1}^N \sum_{m=1}^M z_{nm} \exp \left\{ -2\pi i \left[\frac{(n-1)(s-1)}{N} + \frac{(m-1)(p-1)}{M} \right] \right\} \right|^2 \quad [1]$$

where the second term in Eq. 1 is valid for a sampled profile with N and M sample positions in the two directions. The wavenumber $K \equiv |\mathbf{K}|$ refers to the spatial wavelengths making up the surface profile $z(\mathbf{r})$. Furthermore, $d_x = L_x/(N-1)$ and $d_y = L_y/(M-1)$ with L_x and L_y referring to the scan length in the two directions, $K_x = 2\pi s/Nd_x$ with $s = 1, 2, \dots, N/2$, and $K_y = 2\pi p/Md_y$ with $p = 1, 2, \dots, M/2$. This PSD function has the dimension of (length)⁴.

The PSD function describes two aspects of the surface roughness: the spread of heights from a mean plane, and the lateral distance over which these height variations occur, *i.e.*, the different length scales. This is in contrast to the rms roughness value, which only gives the average height variation along the profile, and no lateral information. The PSD function is also important in light scattering theories, since it connects the scattering into a certain angle

* Electrochemical Society Active Member.

^z E-mail: Claes-Goran.Granqvist@angstrom.uu.se

Table I. Outline of contents of sections of this paper.

	Mechanism or property studied	Experimental method to probe the characteristic	Section in paper
Potential (V vs. Li)	Air OCP	Surface roughness	Adsorption on the Surface: Light scattering, AFM measurement and detailed roughness analysis
	3.5	Adsorption on surface	AFM, light scattering
		Roughness evolution ^a	AFM
	0.9	Electrochromic behavior	Spectrophotometry
		Onset of electrodeposition	Light scattering
	0.8	Initial growth mechanism	Potential step technique
		Thick layer growth ^a	AFM
0.3	Composition	XPS, IR, XRD	Film Composition

^a Denotes a recalculation of the potential range from a Pt to a Li reference electrode.

with the spatial wavelengths of the surface through the first-order grating equation.⁵

There is a relation between the PSD function and the rms roughness: the square root of the integral of the PSD function over all wavenumbers K gives the rms roughness value. For a two-dimensional surface, one has⁸

$$\delta^2 = \frac{1}{(2\pi)^2} \int_{\kappa} \int_{\kappa} g(\mathbf{K}) d(\mathbf{K}) = \int_{\frac{1}{2\pi}}^1 \int_{\kappa_{\min}}^{\kappa_{\max}} \mathbf{K} g(\mathbf{K}) d\mathbf{K} \quad [2]$$

where κ is an area in the K plane. The second term is obtained by turning a two-dimensional spectrum of an isotropically rough surface into a one-dimensional representation by averaging over the polar angle, *i.e.*, by assuming azimuthal symmetry.

Note that the minimum and maximum spatial wavenumbers in Eq. 2, K_{\min} and K_{\max} , are functions of the specific method to assess the surface roughness. All experimental techniques have such limits, thereby defining the bandwidth of the roughness spectrum obtained. The bandwidth limits of a profiling instrument are defined by the scan length and twice the smallest increment in the data point spacing. However, if the profiling probe has a lateral resolution exceeding the data point spacing, the bandwidth limit is twice the lateral resolution of the probe.^{9,10} In angular resolved optical measurements, the bandwidth limits are set by the angle intervals covered by the instrument, *i.e.*, only the lateral wavelengths of the rough surface that scatter into collection angles of the instrument are possible to determine. These lateral frequencies are given by the spatial wavenumber K according to⁵

$$K = \frac{2\pi}{\lambda} n_i (\sin \theta_s - \sin \theta_i) \quad [3]$$

Here, θ_i (θ_s) is the polar angle of the incident (scattered) light beam, λ is the wavelength of light, and n_i is the refractive index of the medium wherein the incident light beam propagates. Equation 3 is the first-order grating equation, where K corresponds to 2π times the grating frequency f . This means that the roughness of a surface can be considered to be composed of a summation of sinusoidal surfaces.^{11,12} The grating spacing Δ , in turn, is given by $\Delta = 1/f$. As a consequence, high wavenumbers correspond to small length scales in the surface profile, and low wavenumbers to large-sized surface features.

To conclude, irrespective of which method is used for surface characterization, the bandwidth limits of the instrument, *i.e.*, the range of length scales contributing to the measured parameter, must be taken into account.¹³ Two different measurement techniques are used in this paper: light scattering and AFM. These two methods have different bandwidth limits (measured in μm^{-1}), which are referred to by the subscripts SC and AFM, respectively. Hence, the rms

roughness may be written δ_{SC} or δ_{AFM} , depending on the selected range of length scales.

Light scattering theory.—Scalar scattering theories¹⁴⁻¹⁹ have been formulated for the total integrated scattering from a random rough surface. The total integrated scattering is the normalized scattering, *i.e.*, the ratio between the diffuse transmittance T_d and the total transmittance T_t . Carniglia¹⁹ showed that this ratio is a measure of the rms roughness for a single, dielectric interface by the relation

$$\frac{T_d}{T_t} \approx \left[\frac{2\pi(n_i \cos \theta_i - n_s \cos \theta_r)\delta}{\lambda} \right]^2 \quad [4]$$

where n_s is the substrate refractive index, and θ_r is the refracted angle of the specular beam as given by Snell's law. It is assumed for Eq. 4 that $T_d + T_s = T_t$. There are no details of the angular dependence of the light scattered (or any polarization effects) in Eq. 4; only values for scattering into the entire hemisphere in transmittance are given.

The derivation of the scalar scattering theory assumes small surface slopes, *i.e.*, the ratio of surface rms roughness and correlation length should be small: $\delta/\xi \ll 1$ (or equivalently, $\delta \ll \lambda$ and $\xi \gg \lambda$).²⁰ This implies that the local radius of curvature is small and that variations in reflectance and transmittance due to changes in the local angle of incidence can be neglected. Furthermore, the surface does not shadow itself for nongrazing incidence, and there is no multiple scattering. Two limitations are frequently referred to²⁰ for scalar scattering theory. First, the scalar theory does not consider the polarization in the incident and scattered light. This is a problem for nonnormal incidence and large scattering angles. Second, for correlation lengths that are small compared to the wavelength, the theory fails to predict the scattering at high angles. In this work, these limitations can be neglected since we carry out the measurements at normal incidence, and the upper collecting angle of the instrument is restricted to 70°.

Experimental

Film preparation.—Our films were made by reactive magnetron sputtering of tin or tungsten in a versatile turbomolecular pumped vacuum deposition unit as described elsewhere.^{3,4} Sputtering was performed in an Ar + O₂ mixture at pressures ranging from 30 to 40 mTorr. Both types of films were deposited onto unheated 1 mm thick glass plates precoated with transparent and conducting In₂O₃:Sn (known as ITO) with a resistance/square of less than 20 Ω. The film thickness d , measured by surface profilometry, ranged from 20 to 520 nm. The deposition rate, obtained by dividing d by the sputtering time, was between 7 and 18 nm/min.

Electrochemical experiments.—We used a standard three-electrode cell²¹ with the sample as working electrode and both the reference electrode and counter electrode made of metallic Li foil. Con-

sequently, the potentials in this paper are given with lithium as reference; the only exception is data taken by AFM, in which a platinum reference was used. The electrolyte was 1 M Merck anhydrous Selectipur LiClO_4 with less than 100 ppm H_2O dissolved in Merck anhydrous Selectipur PC with less than 30 ppm H_2O .

The electrochemical experiments were carried out in Ar atmosphere in a glove box with less than 1 ppm water (dew point below -76°C). The electrochemical cell was controlled by an ECO Chemi Autolab instrument or a TopoMetrix potentiostat. The two basic electrochemical techniques used were chronopotentiometry and chronoamperometry.

Dielectric functions.—The refractive index of the electrolyte was determined through transmittance measurements and standard thin-film calculations.²² The calculation was performed for $400 < \lambda < 800$ nm, where the extinction coefficient was low, and the absorption could be neglected. A Cauchy dispersion relation²³ was employed for the refractive index; this is a reasonable assumption for energies above the bandgap, where only electronic transitions take place. Figure 1 shows that the refractive index is ≈ 1.4 , which is in good agreement with tabulated data.²⁴ The optical constants for the SnO_2 and WO_3 electrodes were taken from the literature.^{25,26} Numerical values are given in Fig. 1. Note that both of the oxides have refractive indices of ≈ 2 , which is much larger than that for the electrolyte.

In situ AFM.—AFM studies of the films were performed using a TopoMetrix Discoverer TMX 2000 instrument equipped with an electrochemical cell. Electrical contact to the sample was achieved by attaching it to the instrument platform with silver glue. A platinum wire was used as the reference electrode, and a platinum ring served as the counter electrode. All AFM measurements were performed at room temperature (25°C) with microfabricated pyramidal Si_3N_4 tips (spring constant 0.032 N/m); the applied force was typically less than 0.5 nN.

In all experiments, the sample was mounted in the empty cell, and the surface was imaged in air before the complete cell was transferred to the glove box. The electrolyte was introduced under argon atmosphere in the glove box. The cell was then transferred to the microscope, and the surface was imaged at the open-circuit potential (OCP) before the electrochemical treatment took place.

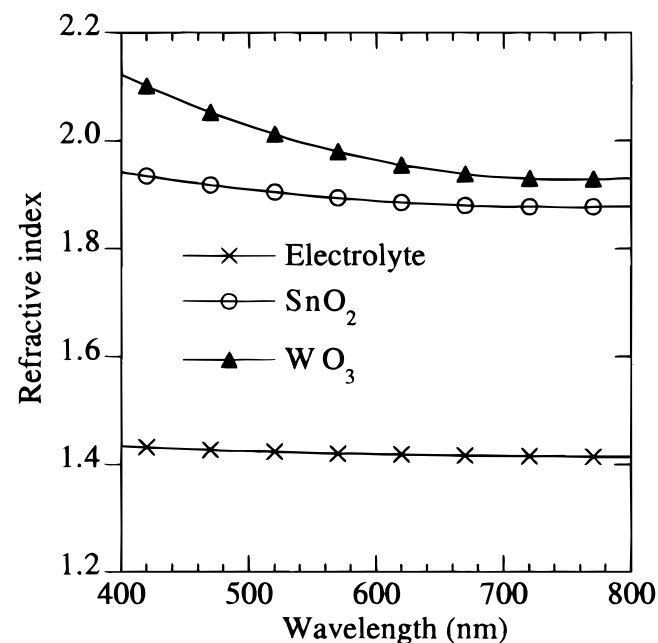


Figure 1. Spectral refractive indices for the electrolyte and for the SnO_2 and WO_3 electrodes.

During a typical experiment of a few hours, the sample was polarized to low potentials by sweeping the potential with a scan rate ≤ 10 mV/s in the cathodic direction. The potential sweep was interrupted when the current reached 0.250 mA, and the sample was held at constant potential under potentiostatic control until the desired charge was attained. The applied potential was then reversed in order to minimize the current, so that the potential was diminished over the interface while the AFM image was captured.

Sequences of surface images were recorded, starting at OCP and at growing layer thicknesses corresponding to increasing levels of charge transfer. Two regimes were studied: first the spontaneously adsorbed layers at OCP and very low levels of intercalation and, second, a regime with a total charge transfer of several C/cm^2 μm wherein an electrodeposited layer was studied.

Surface properties were evaluated over all 300×300 pixel points in the AFM image. The bandwidth limits, K_{\min} and K_{\max} , of the AFM instrument were calculated⁵ to be 0.63 and 133 μm^{-1} for a 10×10 μm scan area, and to be 0.31 and 66 μm^{-1} for a 20×20 μm scan area.

In situ light scattering measurements.—A spectroscopic light scattering experiment was developed to study changes in surface roughness of the electrodes. The electrodes were optically characterized *in situ* in an electrochemical cell, and the diffuse and specular transmittance were recorded using a spectroscopic total integrated scattering (TIS) instrument in the range $330 < \lambda < 970$ nm.²⁷ An outline of the experimental setup is shown in Fig. 2.²⁸ The electrochemical cell is of closed three-electrode type; it was filled with electrolyte in the glove box. The working electrode was placed in the focal point of the light beam in the TIS instrument. The instrument focuses all light that is forward scattered between 2.5 and 70° on one detector, whereas transmitted light, which leaves the hemispherical mirror through the specular port, reaches another detector. The design of the mirror only allows for a very small fraction of the light scattered in the electrolyte to be focused onto the detector, since the focal depth is about a few hundred micrometers at most. A lock-in technique was used for signal acquisition, and the design of the instrument made it possible to detect diffuse reflectance and transmittance values as low as 10^{-5} of the total signal. A computerized data collection facility in combination with the two detectors allowed transmission spectra to be recorded in real time during the experiments.

In the light scattering experiment, the effective rms roughness is unique for each wavelength and thus only includes length scales in the roughness profile covered by the TIS instrument at that specific wavelength. For $\lambda = 400$ nm and for air as the incident medium, K_{\min} and K_{\max} for the TIS instrument were, respectively, 0.69 and 15 μm^{-1} , according to Eq. 3; similarly, for the electrolyte as the incident medium, they were 0.98 and 21 μm^{-1} , respectively.

Compositional and structural analysis.—The samples for compositional and structural analysis were prepared in the glove box in

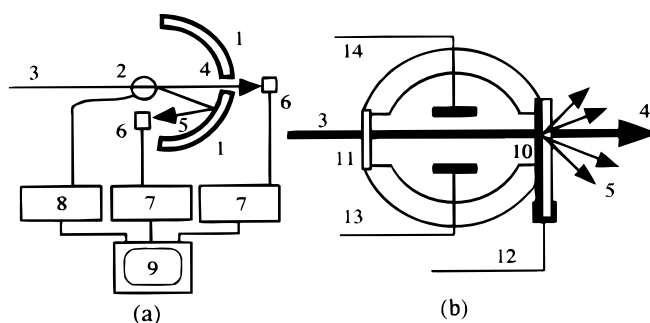


Figure 2. (a) Outline of the total integrated scattering instrument and (b) the electrochemical cell: 1, Focusing mirror; 2, electrochemical cell; 3, incident light beam; 4, specularly transmitted light beam; 5, scattered light cone; 6, detectors with preamplifiers; 7, lock-in amplifiers; 8, electrochemical interface; 9, computer; 10, sample; 11, window; 12, working electrode; 13, counter electrode; 14, reference electrode. After Ref. 28.

an Ar atmosphere. The samples were charged galvanostatically at $\approx 25 \mu\text{A}/\text{cm}^2$ until a potential of 0.3 V vs. Li was reached. They were then cleaned with tetrahydrofuran ($\text{C}_4\text{H}_8\text{O}$) and allowed to dry in the glove box before the analysis.

Infrared (IR) absorption spectroscopy was used to provide compositional analysis. We employed a double-beam Perkin Elmer 983 spectrophotometer in the wavelength range of 500 to 4000 cm^{-1} . The samples were transferred to the spectrophotometer, and the sample was exposed to air for less than a minute before it was mounted and subjected to purging. The IR spectra, recorded at 65° angle of incidence with p-polarized light, were recorded within 5 min.

X-ray diffraction (XRD) at 1° glancing incidence, using a Siemens D5000 unit operated with Cu K radiation, was employed to study the crystal structure of the deposited layer. The samples were transferred fresh from the glove box to the diffractometer and were scanned overnight in air.

X-ray photoelectron spectroscopy (XPS) was used to investigate the composition of the deposited layer. The samples were mounted on a holder in the glove box, and transfer to the XPS apparatus (Perkin Elmer PHI 5500 ESCA) took place without exposing the sample to the ambient.

Adsorption on the Surface

Light scattering.—A change in the optical response was observed during the first hour after the electrolyte was injected into the electrochemical cell. The light scattering increased by a factor of around 10 as the cell was filled with electrolyte. This effect appeared to be instantaneous, and the dynamics could not be studied in detail since the filling of the cell took approximately 5 s. Quantitative values of the increase in roughness may be estimated from Eq. 4, assuming the refractive index of the rough surface layer to be that of either SnO_2 or WO_3 . This is a reasonable simplification since the refractive index of the adsorbed species is expected to be of the same order as that of the thin film,²⁹ and since the rms roughness only depends on the difference in refractive indices, according to Eq. 4.¹⁹

Equation 4 is derived for a semi-infinite rough substrate. In our case, we have a finite substrate thickness, and although the back surface is smooth, there may be multiple reflections in the glass substrate increasing the scattering. For this work, the influence of multiple reflections in the recorded spectra can be ignored. Figure 3 shows evaluations of the rms roughness from the light scattering measurements, *i.e.*, δ_{SC} , obtained with the simplifying arguments just mentioned. Clearly, the roughness, which was 4-9 nm initially for $400 < \lambda < 800$ nm, increased to values between 24 and 40 nm when the electrolyte was introduced. The results are similar for the SnO_2 and WO_3 surfaces.

AFM measurement and detailed roughness analysis.—AFM data showed a significant increase in the surface roughness when the SnO_2 electrode was immersed in the electrolyte, in contrast to the WO_3 electrode, which became smoother. The recorded AFM data were Fourier transformed according to Eq. 1, and PSD functions were calculated. Figures 4 and 5 show data for the SnO_2 and WO_3 electrodes, respectively, taken in air, at the OCP after immersion in electrolyte, and after polarizing the sample to -1.6 or -1.9 V vs. Pt. In both figures, δ_{AFM} denotes the rms roughness from an AFM measurement at a particular scan size, whereas δ_{SC} is the effective rms roughness (calculated by Eq. 3) from the same AFM measurement including the bandwidth limits of the TIS instrument at $\lambda = 400$ nm. It is only for the length scales covered by the TIS measurement at $\lambda = 400$ nm that the spatial wavenumbers overlap with the ones from the AFM measurements so that a direct comparison can be made between the rms roughness from the TIS instrument and the AFM.

The SnO_2 film, reported in Fig. 4, had an initial surface rms roughness of $\delta_{\text{SC}} \pm 6$ nm in air. The surface turned rougher and displayed a rms value of $\delta_{\text{SC}} = 22$ nm after immersion in the electrolyte. Two distributions of grain sizes were detected for the SnO_2 surface in contact with the electrolyte, as apparent from Fig. 4b. They comprise a small-grain distribution of the same lateral and ver-

tical size as in the image of the electrode in air, and an additional large-grain distribution that stood out distinctively in the PSD spectra. After polarizing the SnO_2 electrode below the OCP, the initial incomplete substrate coverage is followed by a more extensive coverage of a large-grained adsorbate, as seen in Fig. 4c. A further lowering of the potential decreased the roughness values to levels comparable to those of the initial surface in air, $\delta_{\text{SC}} = 10$ nm. The roughness values of the AFM images of SnO_2 taken at OCP are in excellent agreement with those from the light scattering measurements as seen in Fig. 3.

The WO_3 film, reported in Fig. 5, had an initial surface rms roughness of $\delta_{\text{SC}} = 12$ nm in air. The surface turned smoother and displayed an rms value of $\delta_{\text{SC}} = 7$ nm after immersion in the electrolyte. The grain distribution is approximately of the same lateral and vertical size as in the image of the electrode in air, and the large grains seen on the SnO_2 film were not observed on the WO_3 film. Polarization to -1.9 V vs. Pt yielded no change in rms roughness, $\delta_{\text{SC}} = 7$ nm. However, the observed rms roughness after immersion in the electrolyte did not conform with the light scattering values presented in Fig. 3. The difference between the adsorption on SnO_2 and WO_3 is further discussed in the sections on Growth of the Electrodeposited Layer and Film Composition.

Onset of Electrodeposition

Electrodeposition was studied *in situ* and in real time using the TIS instrument. A 250 nm thick SnO_2 film immersed in the electrolyte was charged with a current of $1.5 \mu\text{A}/\text{cm}^2$. The results are presented in Fig. 6-8. All the data have been adjusted to compensate for the influence of the transmission of the electrolyte. Figure 6 shows the evolution of the working electrode potential and the measured optical response at $\lambda = 650$ nm during a light scattering experiment. At charge levels (integrated current) less than $100 \text{ mC}/\text{cm}^2 \mu\text{m}$, the potential decreases due to Li intercalation.^{2,3,30} The intercalation causes some electrochromic coloration, manifesting itself as a slightly decreased transmittance. The potential reaches a plateau at about 1.25 V, indicating a phase transition,²¹ and a valence state change was observed by Mössbauer spectroscopy.³¹

The potential drops slowly until it reaches 0.88 V, while the charge increases to $890 \text{ mC}/\text{cm}^2 \mu\text{m}$. The normalized light scattering stays almost constant during this charging. Above $890 \text{ mC}/\text{cm}^2 \mu\text{m}$, the potential increases, *i.e.*, the potential creates a local minimum,

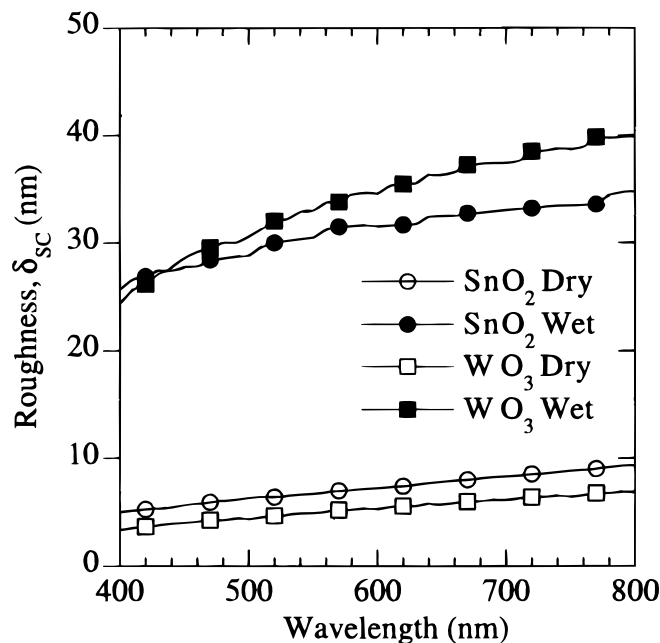


Figure 3. Spectrally dependent rms roughness for SnO_2 and WO_3 surfaces before and after immersion in electrolyte.

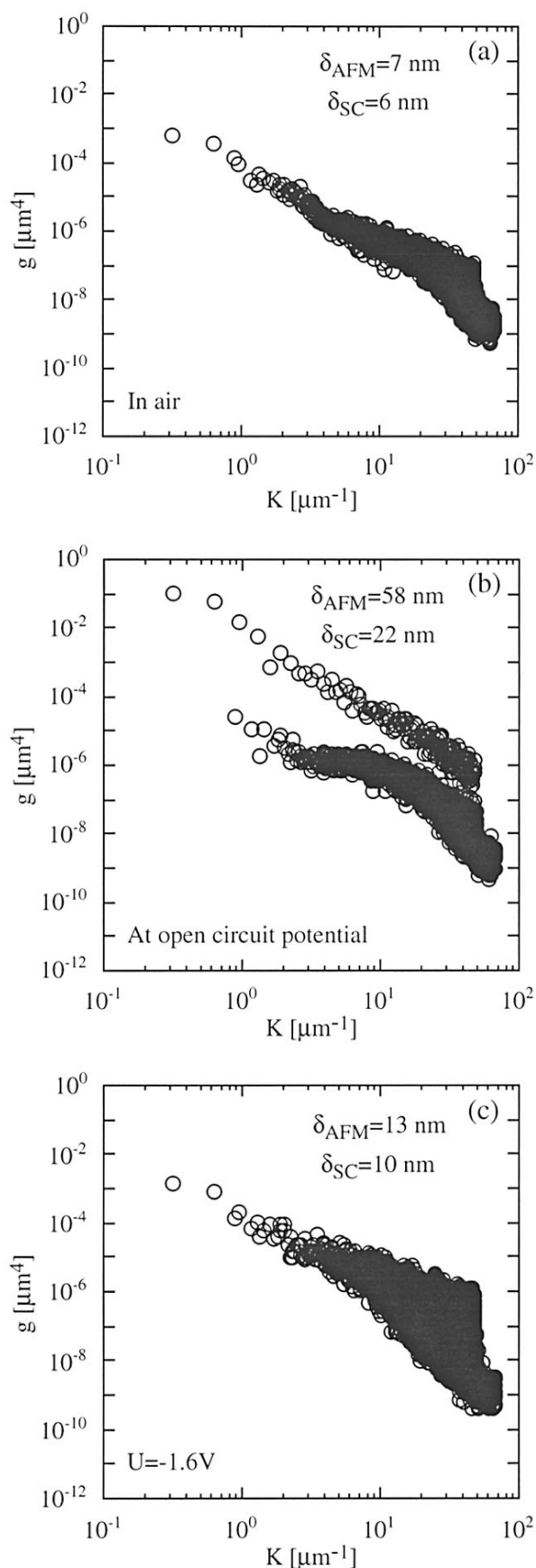


Figure 4. PSD functions from $20 \times 20 \mu\text{m}$ AFM images of SnO_2 . Part (a) refers to the sample in air, part (b) was taken at OCP after immersion in electrolyte, and part (c) after polarization to $U = -1.6$ V vs. Pt. Quantitative values of the roughness, defined in the main text, are given in the figure.

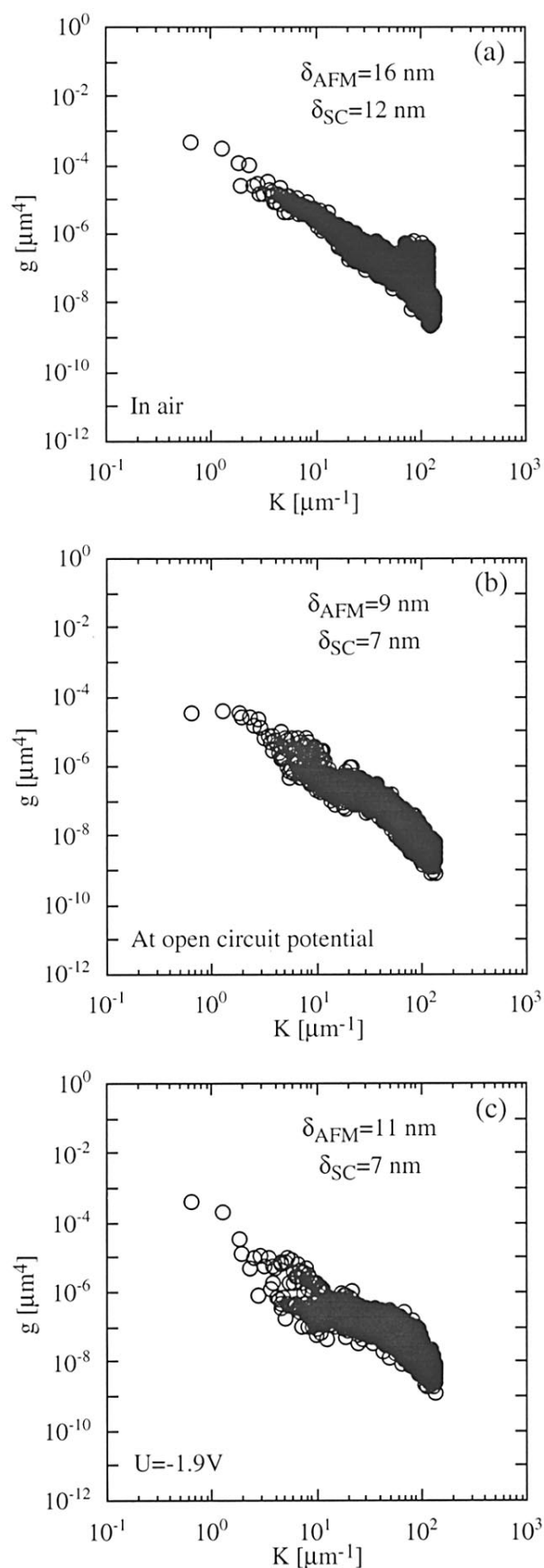


Figure 5. PSD functions from $10 \times 10 \mu\text{m}$ AFM images of WO_3 . Part (a) refers to the sample in air, part (b) was taken at OCP after immersion in electrolyte, and part (c) after polarization to $U = -1.9$ V vs. Pt. Quantitative values of the roughness, defined in the main text, are given in the figure.

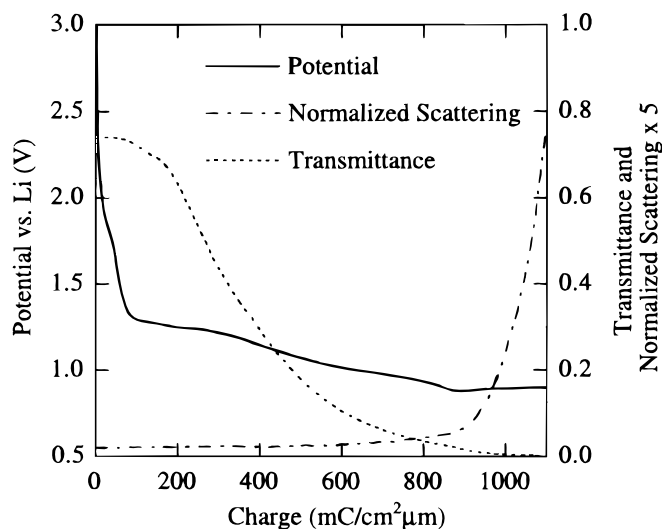


Figure 6. Working electrode potential (solid curve), total transmittance (dotted curve), and normalized scattering multiplied by a factor of 5 (dash-dotted curve) vs. charge for an SnO₂ film. Optical data were taken at a wavelength of 650 nm. Electrodeposition causes a rapid increase of the light scattering at ≈ 890 mC/cm² μ m.

which indicates a phase formation. At this point, the sample starts to scatter light, thereby giving clear evidence for electrodeposition.

Figure 7 illustrates the evolution of the specular transmittance spectra in the $330 < \lambda < 970$ nm range for the SnO₂ film in Fig. 6, and Fig. 8 gives corresponding information on the normalized scattering. Initially, during the first charging up to 70 mC/cm² μ m, the

transmittance is weakly decreased. A higher charging makes the transmittance decrease more rapidly, especially in the blue part of the spectrum, and the film turns visibly brown. A steep decrease in transmittance is discerned around 890 mC/cm² μ m in Fig. 7, and the normalized scattering in Fig. 8 increases sharply at this level of inserted charge. This is where the electrodeposition is initialized.

The behavior of a 380 nm thick WO₃ film charged with a current of 1.5 μ A differs from the result of the SnO₂ films, as apparent from Fig. 9-11. After charging with less than 50 mC/cm² μ m, the transmittance at the wavelength 650 nm is close to zero; see Fig. 9. Figure 10 shows that the transmittance in the red part of the spectrum is close to zero, while the transmittance in the blue region still is significant. This is a signature of the well-documented electrochromism in WO₃ and can be explained in terms of small polaron absorption.¹ The spectral properties change as the intercalation progresses; at 300 mC/cm² μ m, the film attains a brownish appearance. It is conceivable that a substantial number of the available intercalation sites are occupied so that site saturation prevails,³² and at 300 mC/cm² μ m, the intercalation level is estimated to be Li_{1.3}WO₃, well above the upper limit of 0.5 in the site-saturation model. At 540 mC/cm² μ m the potential comes to a local minimum, as apparent from Fig. 9, indicating a phase formation or phase transformation. Above 540 mC/cm² μ m, the transmittance goes rapidly to zero. There is an accompanying growth of the normalized light scattering, clearly seen in Fig. 11. These data give evidence for electrodeposition.

The light scattering spectra of SnO₂ and WO₃ differ substantially at the onset of electrodeposition. The data for WO₃ are very distinct at the point of electrodeposition, which indicates that the nucleation rate is very high, so high that the crystals grew to a size detectable even with long wavelengths within a 20 min interval between two successive spectral measurements. However, the scattering spectra of SnO₂ show a smooth onset that can be detected first at

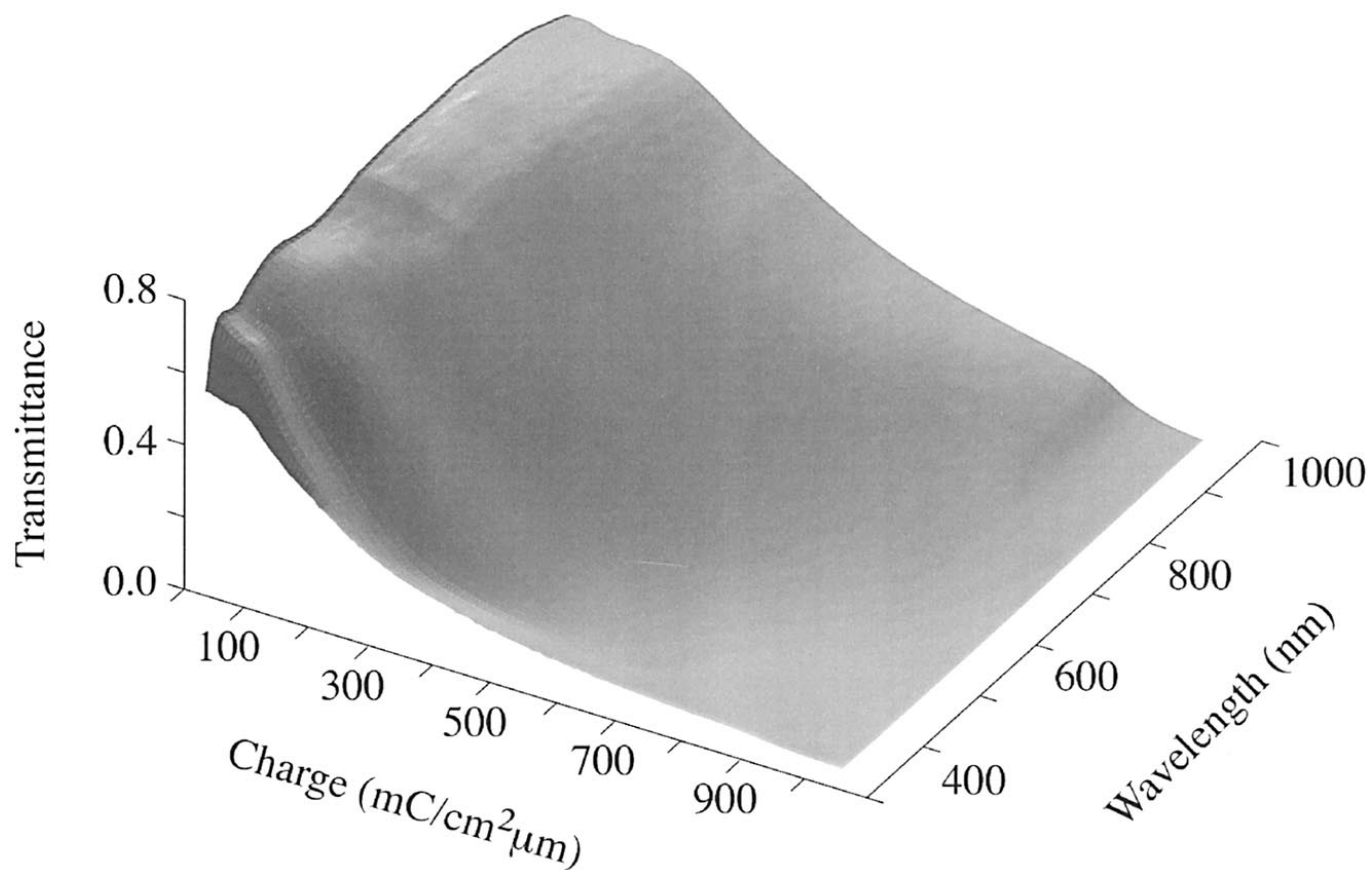


Figure 7. Specular transmittance of an SnO₂ electrode as a function of wavelength and charge.

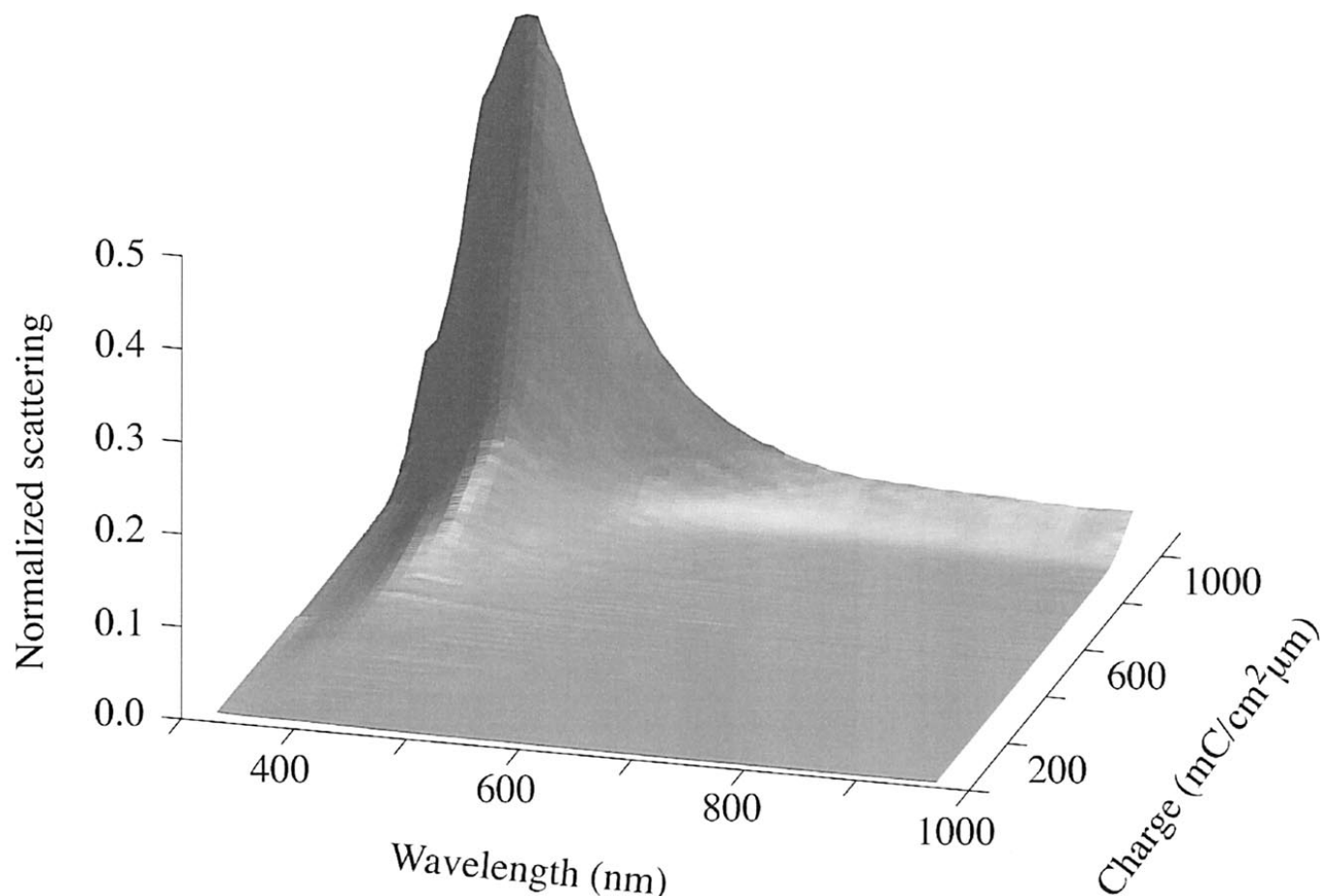


Figure 8. Normalized scattering of an SnO_2 electrode as a function of wavelength and charge. To gain clarity, the axes for wavelength and charge are not the same as in Fig. 7.

short wavelengths. With a high total charge, the total signal is also very small, *i.e.*, the total transmittance is low, and thus the relative error in the normalized scattering is larger. We conclude that the

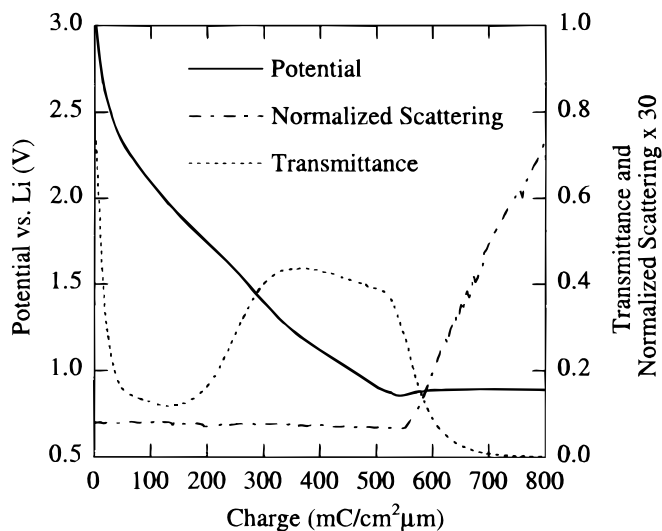


Figure 9. Working electrode potential (solid curve), total transmittance (dotted curve), and normalized scattering multiplied by a factor of 30 (dash-dotted curve) vs. charge for a WO_3 film. Optical data were taken at a wavelength of 650 nm. Electrodeposition causes a rapid increase of the light scattering at $\approx 540 \text{ mC/cm}^2 \mu\text{m}$.

nucleation and growth of crystals are slower on SnO_2 than on WO_3 . The onset of electrodeposition was detected at $0.87 \pm 0.03 \text{ V vs. Li}$ for both the SnO_2 and the WO_3 electrodes.

Growth of the Electrodeposited Layer

The light scattering technique described above is a novel method, and the application of AFM in electrochemistry has only recently become routine. We have also adopted more traditional techniques in electrochemistry to obtain complementary information. One technique able to detect film growth on a surface relies on the application of a potential step. This technique has been applied, and we show a response that can be assigned to a film formation on the surface. AFM was used to study the initial adsorption on the surface, and it has also been applied to study the dynamics of the film growth at a stage when the film has reached a substantial thickness.

Potential step technique.—A potential step technique was applied to all samples. The chronoamperometric response was studied after steps from a potential $U_{\text{high}} = 4.5 \text{ V}$ to $U_{\text{low}} = 1.5 \text{ V vs. Li}$. The potential was held for 60 s at each step, and each step was repeated twice. In the next cycle, U_{low} was decreased by 0.1 V to $U_{\text{low}} = 1.4 \text{ V}$. After a sequence of steps, the sample was relaxed at the OCP for 2 min before continuing to the next potential. Sequences of this kind were repeated until steps between $U_{\text{high}} = 4.5 \text{ V}$ and $U_{\text{low}} = 0.6 \text{ V}$ were reached. Figure 12 shows the current response of a 20 nm thick SnO_2 film with an area of $\approx 0.8 \text{ cm}^2$. At $U_{\text{low}} = 1.2 \text{ V}$, the current decreases monotonically, while for $U_{\text{low}} = 1.1 \text{ V}$ and yet lower potentials, there is a short-time increase in the current.

The thinnest SnO_2 films showed a potential response that can be modeled with a theory for nucleation and growth of monolayers on a surface. Current time ($I-t$) transients, measured in the potential step

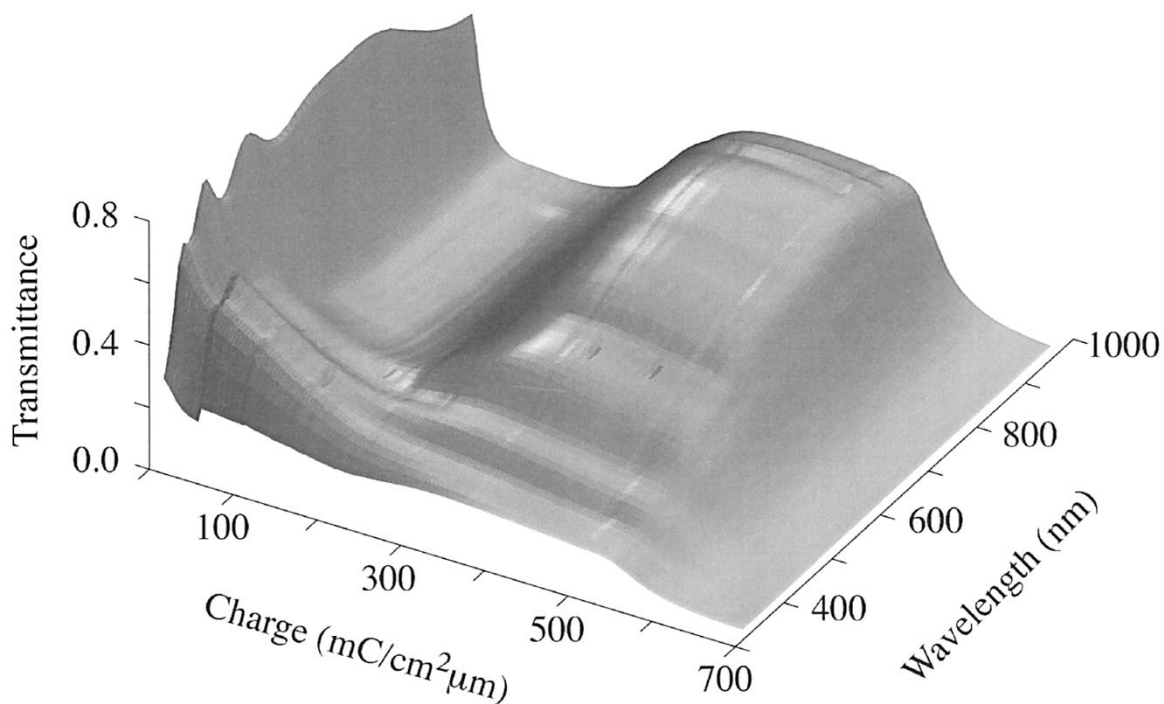


Figure 10. Specular transmittance of a WO₃ electrode as a function of wavelength and charge.

experiments described above, were fitted to an equation²¹ for growth of a monolayer according to

$$\frac{I}{I_m} = \frac{t^2}{t_m^2} \exp\left(-\frac{2(t^3 - t_m^3)}{3t_m^3}\right) \quad [5]$$

where I_m is the current at the maximum, reached after a time t_m . The equation corresponds to a progressive nucleation of growth centers.

Figure 13 shows $I-t$ transients of the film reported in Fig. 12 with the current peak value normalized to unity. The agreement between the experimental data points and the curves calculated from Eq. 5 for progressive nucleation and growth of two-dimensional precipitates is good. However, the area under the curve with $U_{low} = 1.1$ V in Fig. 13

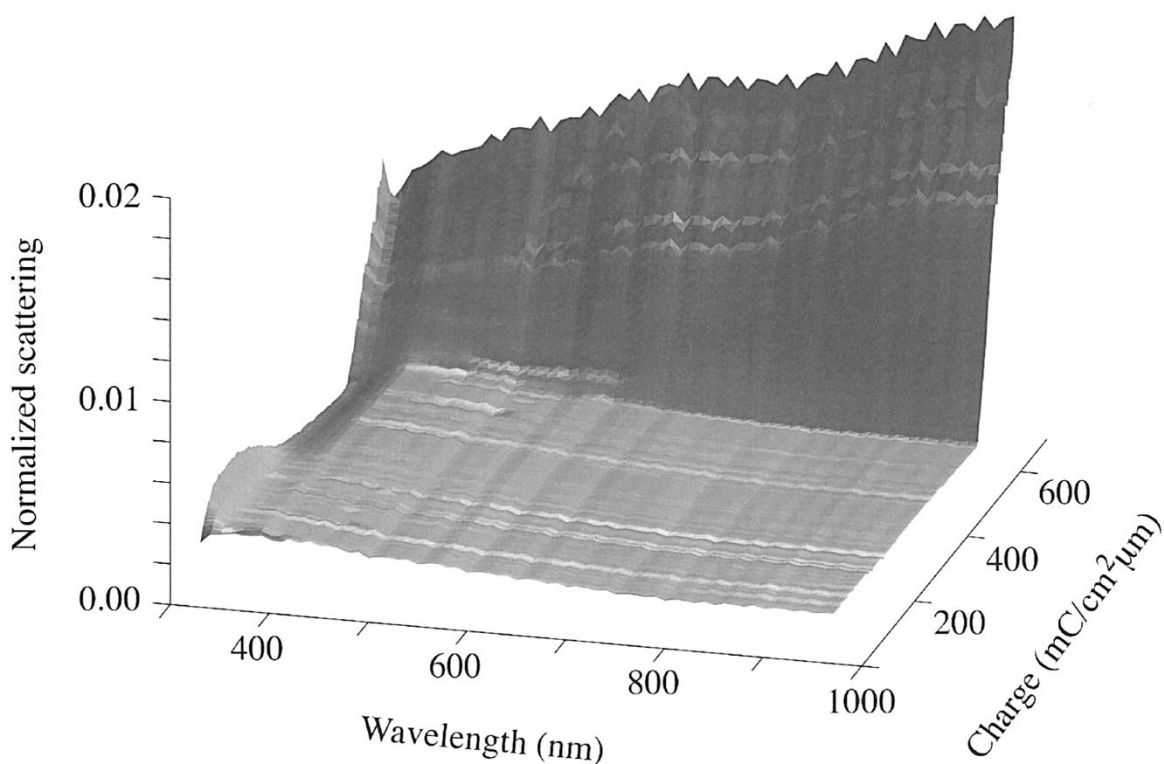


Figure 11. Normalized scattering of a WO₃ electrode as a function of wavelength and charge. To gain clarity, the axes for wavelength and charge are not the same as in Fig. 10.

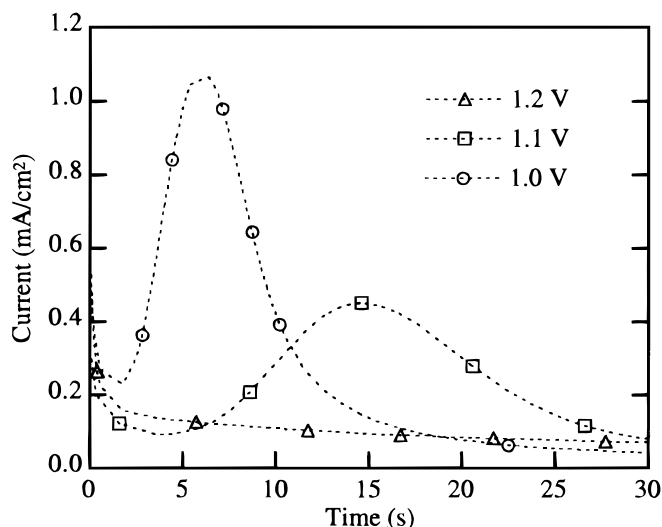


Figure 12. Current vs. time for potential steps applied to a 20 nm thick SnO_2 film. The potential steps are from 4.5 V vs. Li to the values indicated in the figure.

corresponds to a charge of about 6 mC/cm^2 . As the charge yielding a monolayer of a deposit ought to be significantly smaller than this charge (the deposition of a monolayer of lithium metal by reduction of Li^+ would require a charge of only $\approx 0.2 \text{ mC/cm}^2$), it is likely that the transient in Fig. 13 is associated with the deposition of a number of subsequent monolayers. Although the magnitudes of the t_m (and to some extent also the I_m) values depended on the history of the electrodes, these variations did not seem to influence the nucleation and growth mechanism, and the fits to Eq. 5 are convincing.

Transients similar to those in Fig. 13 were only seen in very thin SnO_2 films (20 nm), but we see no reason why the same nucleation and growth mechanism should not pertain to the thicker films as well. For the thicker SnO_2 films, and the WO_3 films for which the intercalation is a dominant process, we applied a model describing the release of ions from a layer on the surface and subsequent migration of these ions into the film to explain the behavior.^{33,34}

Growth of thick layers.—The subsequent growth of a thick deposited layer was studied by AFM. Figure 14 shows film growth during electrodeposition on an SnO_2 electrode. We used a scan size

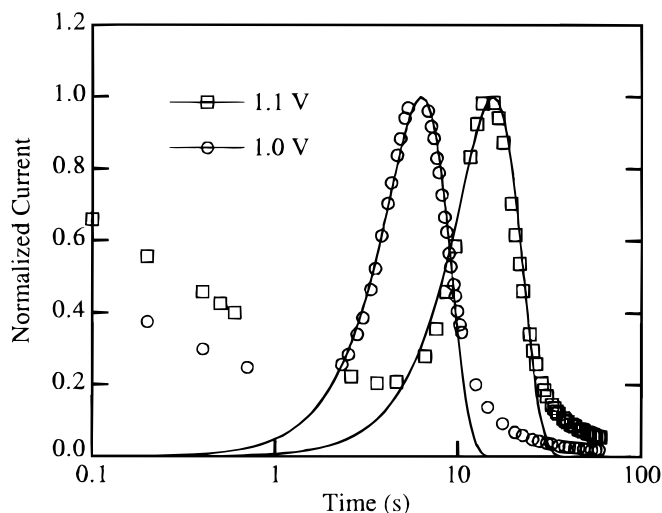


Figure 13. Time-dependent current during electrodeposition on a 20 nm thick SnO_2 electrode as obtained from measurements (symbols) and from a theory for progressive nucleation of growth centers (solid lines).

of $10 \times 10 \mu\text{m}$. The deposit initially forms a homogeneous layer. Then, at certain sites distributed several micrometers apart, some crystallites start to grow. This is seen in the PSD diagrams as an increased intensity at low spatial wavenumbers, *i.e.*, at long length scales in the surface profile. In a final growth stage, the background, *i.e.*, the area between these large bumps, becomes rougher. The latter effect is detected in the PSD plots as increased intensity at short wavenumbers or, equivalently, at high wavenumbers. Thus, the growth process is preferential in thick layers, where favored sites produce large crystals growing faster than the background.

Figure 15 shows the growth of precipitates on a WO_3 film. This time we used $20 \times 20 \mu\text{m}$ squares. It is apparent from the second frame that an additional scan of $10 \times 10 \mu\text{m}$ is clearly visible in the $20 \times 20 \mu\text{m}$ image. Hence, the precipitate did not adhere to the WO_3 film as well as it did to the SnO_2 film, and the movement of the tip influenced the surface. In both Fig. 14 and 15, δ_{AFM} denotes the rms roughness from the AFM measurement including the bandwidth limits at that particular scan size.

Film Composition

We studied the composition and structure of the precipitate to more fully understand the onset of the deposition from the electrolyte. The precipitate is formed in a very complex system; a good review on the subject is given by Aurbach.³⁵ The emphasis in our work is on the two *in situ* methods; the compositional and structural investigation is used only to support those results. Specifically, we used three *ex situ* methods: IR absorption spectroscopy, XRD, and XPS. We prepared samples by polarizing the SnO_2 and WO_3 films to a potential as low as 0.3 V vs. Li. This is 0.5 V lower than the onset potential for the deposition, and our technique gave us a thick enough layer for analysis with the three mentioned techniques.

IR absorption spectroscopy.—Measurements in the IR by use of a double-beam Perkin Elmer 983 spectrophotometer yielded a low reflectance, especially above 1500 cm^{-1} . This is due not only to adsorption but also to light scattering from surface roughness. The particles seen in the AFM images reported in Fig. 14 and 15 have lateral sizes up to $5 \mu\text{m}$ and vertical peak-to-peak values of about $1 \mu\text{m}$. Hence, a significant light scattering is expected in the IR wavelength range.

The surfaces of the deposited layers were very reactive, and exposure of the samples to air for a day yielded a significant change of the spectra, whose absorption bands became more prominent. We studied the absorption spectra for fresh samples (exposed to air only for some minutes) as well as for aged samples stored for a day in air.

The fresh films yielded measured absorption bands indicating the presence of lithium alkyl carbonate species, ROCO_2Li , where R is an alkyl group.³⁶ In the aged films, the measured absorption bands indicated the presence of Li_2CO_3 .^{36,37} Hence, based on these *ex situ* measurements, we conclude that lithium alkyl carbonate species are one of the products in the freshly deposited layer, and that lithium carbonate is one of the products in the aged layer.

XRD.—An X-ray diffractogram of an electrodeposited layer showed clear evidence for the ITO layer on the substrate. No structures due to the SnO_2 or WO_3 films were seen, and hence these films can be characterized as amorphous.^{2,3} The deposited layer did not show any specific X-ray features. This is consistent with an inhomogeneous composition.

XPS.—Our XPS spectra showed an indistinct composition, and it appears that there is no unique surface layer formed during the deposition. The layer on the WO_3 electrode had the overall composition 31 atom % Li, 29 atom % C, and 39 atom % O, while the layer on the SnO_2 electrode showed 21 atom % Li, 40 atom % C, and 36 atom % O. There were traces of Cl on both electrodes, of some Ca and W on the WO_3 electrode, and of some F and Sn on the SnO_2 electrode. We noted a small variation in the composition between the bumps and the flat surface (*cf.* Fig. 14 and 15), and the bumps contained less Li.

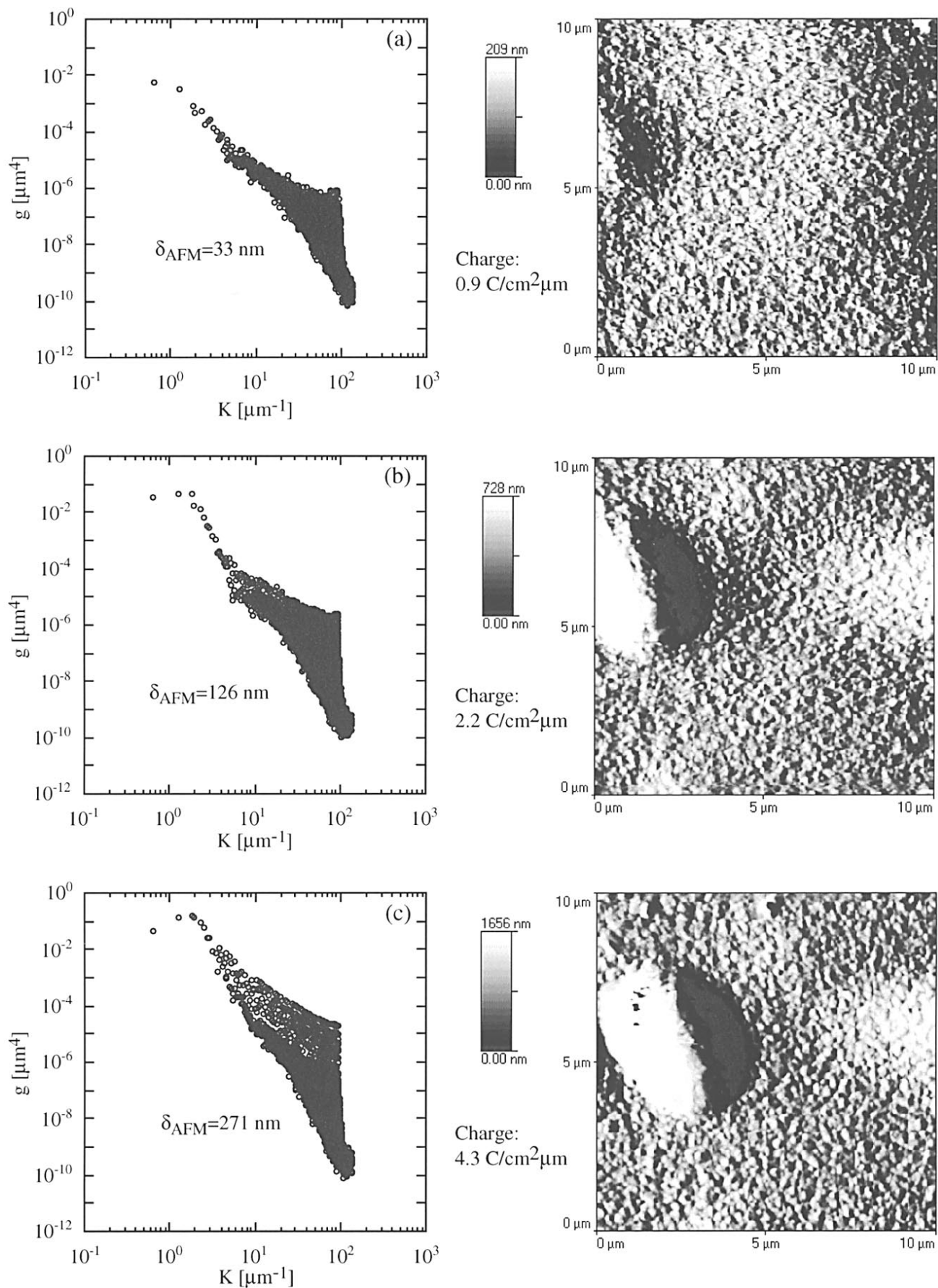


Figure 14. Evolution of morphology during electrodeposition on an SnO₂ film. AFM images of size $10 \times 10 \mu\text{m}$ are shown on the right, and corresponding PSD functions are shown on the left. The data were recorded for the shown magnitudes of charge transfer.

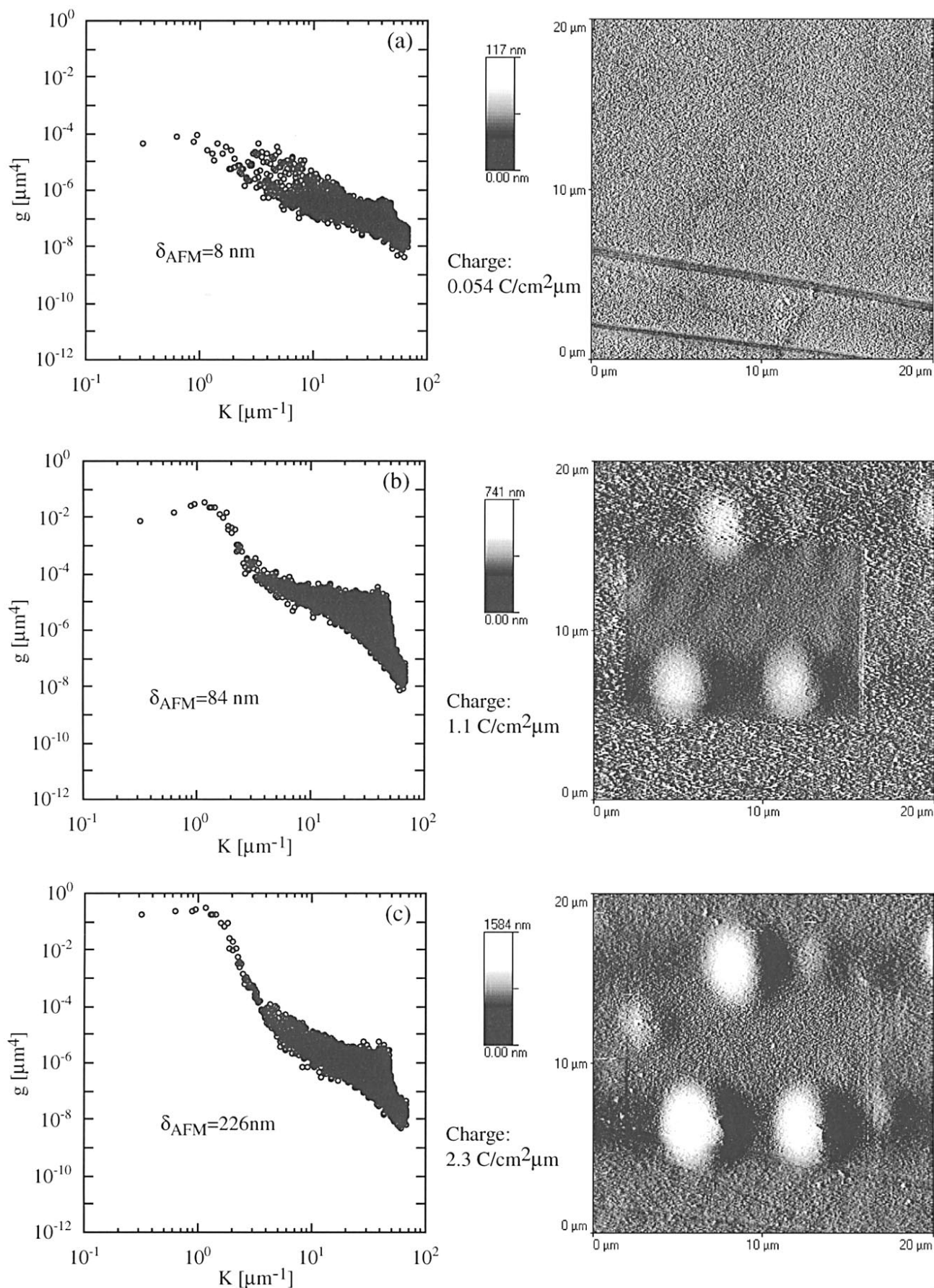


Figure 15. Evolution of morphology during electrodeposition on a WO_3 film. AFM images of size $20 \times 20 \mu\text{m}$ are shown on the right, and corresponding PSD functions are shown on the left. The data were recorded for the shown magnitudes of charge transfer.

Conclusions

The main objective of this investigation was to study adsorption and electrodeposition on SnO₂ and WO₃ electrodes with an *in situ* light scattering technique and with *in situ* AFM. We established the potential range that can be used for electrochemical experiments and the limitation set by the electrolyte. We decisively determined whether the change in the observed optical modulation is due to electrodeposition or electrochromism.

Both light scattering and AFM showed the same increase in surface roughness immediately after the SnO₂ electrode was immersed in the electrolyte. The behavior of the WO₃ electrode differed, and no large grains were seen in the AFM. The first small signs of deposition were detected with a potential step technique at a potential of 1.1 V vs. Li. This coincides³⁸ with the potential where reactions including H₂O occur, and we believe that small amounts of water present in the electrolyte were reduced here.

The onset of a massive decomposition of the electrolyte, and the resulting electrodeposition, were detected at 0.87 ± 0.03 V vs. Li for both the SnO₂ and the WO₃ electrodes. The specific value of the potential depends on the film composition as well as on the composition and purity of the electrolyte. The growth mode of the initially deposited layer could be understood as a progressive growth of layers, while the later stages of the deposition were characterized by a preferential evolution of large crystals. These crystals were detected using both light scattering and AFM techniques.

The investigation of the composition of the deposited layer is not conclusive. However, IR spectroscopy with p-polarized light indicates that ROCO₂Li is a likely component in the compound formed during deposition. IR spectra as well as XPS data led to the conclusion that the SnO₂ and WO₃ electrodes promoted slight differences in the growth and composition of the surface layer.

Uppsala University assisted in meeting the publication costs of this article.

References

1. C. G. Granqvist, *Handbook of Inorganic Electrochromic Materials*, Elsevier, Amsterdam (1995).
2. C. G. Granqvist, *Sol. Energy Mater. Sol. Cells*, **60**, 201 (2000).
3. J. Isidorsson and C. G. Granqvist, *Sol. Energy Mater. Sol. Cells*, **44**, 375 (1996).
4. A. Azens, C. G. Granqvist, E. Pentjuss, J. Gabrusenoks, and J. Barczynska, *J. Appl.*

- Phys.*, **78**, 1968 (1995).
5. J. C. Stover, *Optical Scattering: Measurement and Analysis*, SPIE, Bellingham, WA (1995).
6. D. Rönnow, Ph.D. Thesis, Uppsala University, Sweden (1996).
7. J. M. Elson and J. M. Bennett, *Appl. Opt.*, **34**, 201 (1995).
8. J. M. Elson, J. P. Rahn, and J. M. Bennett, *Appl. Opt.*, **22**, 3207 (1983).
9. E. L. Church, T. V. Vorburger, and J. C. Wyant, *Opt. Eng.*, **24**, 388 (1985).
10. E. L. Church and P. Z. Takacs, *Proc. SPIE-Int. Soc. Opt. Eng.*, **1009**, 46 (1989).
11. J. C. Stover, in *Laser Induced Damage in Optical Materials*, p. 163, National Bureau of Standards (1974).
12. J. C. Stover, *Appl. Opt.*, **14**, 1796 (1975).
13. J. M. Bennett and L. Mattsson, *Introduction to Surface Roughness and Scattering*, Opt. Soc. Am., Washington, DC (1999).
14. H. E. Bennett and J. O. Porteus, *J. Opt. Soc. Am.*, **51**, 123 (1961).
15. H. E. Bennett, *J. Opt. Soc. Am.*, **53**, 1389 (1963).
16. J. Ebert, H. Pannhorst, H. Küster, and H. Welling, *Appl. Opt.*, **18**, 818 (1979).
17. J. M. Eastman, Ph.D. Thesis, University of Rochester, Rochester, NY (1974).
18. H. Davies, *Proc. IEE*, **101**, 209 (1954).
19. C. K. Carniglia, *Opt. Eng.*, **18**, 104 (1979).
20. J. M. Zavislan, *Appl. Opt.*, **30**, 2224 (1991).
21. R. Greef, R. Peat, L. M. Peter, D. Pletcher, and J. Robinson, *Instrumental Methods in Electrochemistry*, Ellis Horwood, New York (1990).
22. O. S. Heavens, *Optical Properties of Thin Solid Films*, Dover, New York (1965).
23. W. J. Tropf, M. E. Thomas, and T. J. Harris, in *Handbook of Optics*, Vol. II, M. Bass, Editor, Chap. 33, McGraw-Hill, New York (1995).
24. T. J. Bruno and P. D. N. Svoronos, in *CRC Handbook of Basic Tables for Chemical Analysis*, p. 89, CRC, Boca Raton, FL (1989).
25. K. v. Rottkay, M. Rubin, and S.-J. Wen, *Thin Solid Films*, **306**, 10 (1997).
26. J. Isidorsson, C. G. Granqvist, K. v. Rottkay, and M. Rubin, *Appl. Opt.*, **37**, 7334 (1998).
27. D. Rönnow and E. Veszelei, *Rev. Sci. Instrum.*, **65**, 327 (1994).
28. D. Rönnow and J. Isidorsson, *Solid State Commun.*, **100**, 695 (1996).
29. *CRC Handbook of Chemistry and Physics*, 73rd ed., D. R. Lide, Editor, p. 4, CRC, Boca Raton, FL (1992).
30. M. Strømme, J. Isidorsson, G. A. Niklasson, and C. G. Granqvist, *J. Appl. Phys.*, **80**, 233 (1996).
31. J. Isidorsson, C. G. Granqvist, L. Häggström, and E. Nordström, *J. Appl. Phys.*, **80**, 2367 (1996).
32. M. Denesuk and D. R. Uhlmann, *J. Electrochem. Soc.*, **143**, L186 (1996).
33. G. Greeuw and B. J. Hoenders, *J. Appl. Phys.*, **55**, 3371 (1984).
34. M. Strømme Mattsson, J. Isidorsson, and T. Lindström, *J. Electrochem. Soc.*, **146**, 2613 (1999).
35. *Nonaqueous Electrochemistry*, D. Aurbach, Editor, p. 289, Marcel Dekker, New York (1999).
36. D. Aurbach, M. Daroux, P. Faguy, and E. Yeager, *J. Electrochem. Soc.*, **134**, 1611 (1987).
37. F. A. Miller and C. H. Wilkins, *Anal. Chem.*, **24**, 1253 (1952).
38. D. Aurbach, M. Daroux, P. Faguy, and E. Yeager, *J. Electroanal. Chem.*, **297**, 225 (1991).